Title
Microturbulence Suppression by Alfvén Eigenmodes in the DIII-D Tokamak

Journal
Physical Review Letters, 135(26)

ISSN
0031-9007

Authors
Du, XD
Heidbrink, WW
Yan, Z
et al.

Publication Date
2025-12-31

DOI
10.1103/fdnb-ycz7

Peer reviewed

*Published as: Du et al., *Phys. Rev. Letters* **135**, 265101 (2025).
doi:10.1103/fdnb-ycz7

Microturbulence Suppression by Alfvén Eigenmodes in the DIII-D Tokamak

X.D. Du,[1] W.W. Heidbrink,[2] Z. Yan,[3] P.H. Diamond,[4] G.R. McKee,[3] L. Schmitz,[5]
M.A. Van Zeeland,[1] H.Q. Wang,[1] M.E. Austin,[6] L. Liu,[6] K. Callahan,[2,7] and N. Shi[1]

[1] *General Atomics, P.O. Box 85608, San Diego, California 92186-5608, USA*
[2] *University of California, Irvine, California 92697, USA*
[3] *University of Wisconsin-Madison, Madison, Wisconsin 53706-1687, USA*
[4] *University of California San Diego, La Jolla, California 92093-0319, USA*
[5] *University of California-Los Angeles, Los Angeles, California 90095, USA*
[6] *University of Texas-Austin, Austin, Texas 78712, USA*
[7] *Oak Ridge Institute for Science and Education, Oak Ridge, Tennessee 37830, USA*

(Dated: November 16, 2025)

Mitigation and suppression of low-k turbulence are observed during the nonlinear evolution of toroidicity-induced Alfvén eigenmodes (TAEs) in DIII-D experiments. Turbulence mitigation begins when the dominant TAE starts to depart from the typical shear Alfvén wave polarization. TAE activity then evolves into a new state, characterized by more discrete coherent modes, increased total amplitude, and more localized radial structures. During this transition, a narrow shear flow layer forms, driven by an enhanced Reynolds stress force, with a shearing rate that exceeds the local turbulence decorrelation rate, leading to a full turbulence suppression. These observations indicate the imbalance between Reynolds and Maxwell stress forces during the nonlinear evolution of the TAE and their important roles in shear flow generation and turbulence reduction.

PACS numbers:

As nuclear fusion research advances towards the era of burning plasmas, the traditional division of plasma studies into distinct areas of thermal particles and energetic particles (EPs), and their associated confinement, is becoming increasingly inadequate. In burning plasma regime, drift waves driven by thermal particles, which govern thermal plasma confinement [1, 2], coexist with Alfvén eigenmodes (AEs) excited by fusion-born α particles [3–9]. Theoretical studies predict cross-scale, nonlinear interaction among EPs, AEs and low-frequency drift waves, mediated by zonal flow and/or zonal fields [10–14].

In present magnetically-confined fusion devices, improved thermal confinement in the presence of EPs and EP-driven instabilities has been reported across several experiments, such as ASDEX-Upgrade [15], LHD [16, 17], DIII-D [18, 19], JET [20] and KSTAR [21]. Interpretations of these observations have largely relied on numerical modeling. Proposed physics mechanisms include the fast ion dilution effect [21, 22], enhanced zonal flow due to fast ions [23, 24], resonant interaction between fast ions and drift waves [15], non-ambipolar EP transport [16–19], zonal flow driven by EP-driven instabilities [25–27] or a combination thereof. However, a comprehensive understanding grounded in detailed experimental measurements remains elusive, primarily due to the persistent challenges in diagnosing key plasma parameters relevant to these multi-scale, nonlinear interactions.

In this Letter, we present experiments in the DIII-D tokamak that demonstrate mitigation and suppression of low-k turbulence, induced by toroidicity-induced AEs (TAEs). We present direct experimental evidence that the suppression of low-k turbulence results from the formation of a narrow, strong shear flow layer, whose shearing rate exceeds the observed turbulence decorrelation rate. Importantly, the mitigation of low-k turbulence precedes the formation of this shear flow layer and coincides with an abrupt deviation of the TAE from the typical shear Alfvén wave polarization. This deviation reflects a breakdown in the balance between Reynolds stress (RS) and Maxwell stress (MX) force during the nonlinear evolution of TAE, which plays an important role in the mitigation and suppression of low-k turbulence.

Experimental data - The experiment is carried out near the plasma edge at $r/a \sim 0.7$, a location chosen for the coexistence of strong low-k turbulence and TAE under a monotonic safety factor (q) profile at toroidal field of $B_t = -2.1$ T. The beam emission spectroscopy (BES) system [28, 29] simultaneously measures the density fluctuations induced by TAE and by low-k turbulence. The system has 64 channels arranged in an 8×8 array in the R-Z plane that covers a radial range R from 2.142 m to 2.208 m ($r/a \sim 0.65$ to 0.82) and vertical range Z from -0.042 m to 0.065 m. The setup of the BES system and plasma poloidal cross section are shown in End Matter.

As shown by the solid arrow in Fig. 1(a), a dominant $n = 4$ TAE with a coherent frequency of $f \sim 120$ kHz is observed by a BES channel at $R = 2.142$ m and $Z = -0.012$ m. As this TAE gradually disappears after ~ 0.6 s, multiple discrete coherent modes emerge across a broader frequency range of ~ 90 to 145 kHz, comprising, at least, well-identified three $n = 4$ and two $n = 3$ modes (see the dashed arrows). Note that the n is determined from a toroidal array of the magnetics [30] and the details are included in End Matter. On the other hand, the microturbulence, characterized by a broadband frequency

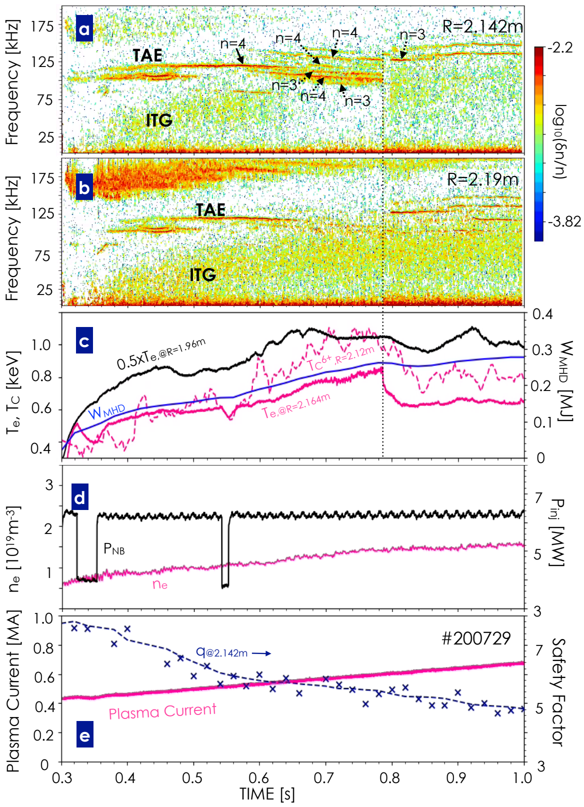

FIG. 1: Time evolution of normalized density fluctuations measured by BES at $(R, Z) = (2.142, -0.012)$ m (a) and $(2.19, -0.012)$ m (b), respectively, (c) stored energy, electron and carbon temperatures, (d) injected neutral beam power and line-averaged density, and (e) safety factor and plasma current. The vertical dotted line marks the end of the turbulence suppression phase, as also indicated in Figs. 3..

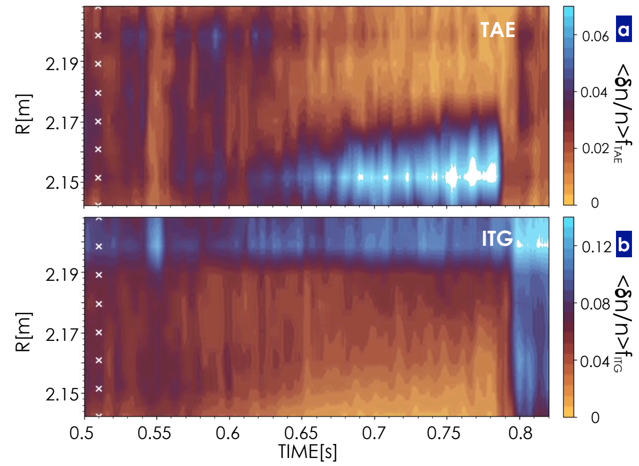

FIG. 2: Time evolution of $\delta n/n$ induced by TAE (a) and ITG (b) from radial range 2.142 m to 2.21 m, measured by BES system. The mode amplitudes are obtained by integrating over the corresponding TAE and ITG frequency bands with high coherence (> 0.8) and relevant phase shift between a BES pair, separated poloidally at the same radial location.

spectrum, is observed in the lower frequency range of $f < 100$ kHz by the same BES channel. The $\delta n/n$, induced by the turbulence, decreases around 0.57 s and nearly complete suppression occurs between ~ 0.65 s and ~ 0.78 s, lasting about four energy confinement times. The turbulence re-emerges at ~ 0.782 s, as indicated by vertical dotted lines in Fig. 1.

It is noteworthy that the mitigation/suppression of the turbulence is found in a very narrow radial region. For example, as seen from Fig. 1(b), $\delta n/n$ measured by the BES channel at $R = 2.19$ m and $Z = -0.012$ m, i.e., only ~ 5 cm farther outward, exhibits distinctly different evolution. The turbulence persists with no indication of the mitigation or suppression between 0.6 s and 0.78 s, and meanwhile, only two weak TAEs are observed. The spatial resolution of BES system, obtained from the point spread function [31] accounting for beam-magnetic field geometry, optics and finite-excited state lifetime effects, is typically 1-2 cm. For the BES channel in Fig. 1(a), it is ~ 1.9 cm radially and ~ 1.2 cm vertically.

Figure 2 provides a comprehensive view of the temporal evolution of TAEs and the turbulence across the full radial region monitored by 8 channels of BES, whose positions are labeled by crosses. In Fig. 2(a), prior to ~ 0.65 s, the TAE exhibit a broad radial structure spanning from $R = 2.142$ m to 2.208 m. Afterwards, the radial width of the mode structure abruptly narrows, while the amplitudes of the TAEs, integrated over 90 to 145 kHz, increase significantly. The radial structure also expands outward by 1 cm before suddenly disappearing at ~ 0.78 s, just prior to the ITG recovery at ~ 0.8 s. The TAE with a global structure then reappears, but at much lower amplitudes. Additional examples of repeated transitions between global, low-amplitude TAEs and localized, high-amplitude, TAE are shown in Figs. 8 and 9 of End Matter. In comparison, Figure 2(b) shows that the turbulence is present across all BES channels with stronger amplitudes at larger radii, before ~ 0.6 s. An anti-correlation relationship between turbulence and TAE activities is observed: (1) During strong TAE activity between 0.65 s and 0.79 s, the turbulence suppression occurs at $R \sim 2.14$ m; (2) The turbulence mitigation extends radially outward up to 2.17 m, temporally and spatially coinciding with regions of increased TAE amplitudes. (3) beyond ~ 2.17 m, when TAE amplitudes decrease, ITG amplitudes increase.

Images of turbulent eddies, measured by BES system, show the poloidal wave numbers of $k_\theta \sim 0.8$ cm^{-1} and tilted structures during the suppression at $R = 2.143$ m. CGYRO simulations[32] identify this low-k turbulence as ion temperature gradient (ITG) modes. It finds that the ITG modes with $k_\theta = 0.8 - 1.4$cm^{-1} are primarily responsible for the largest electron and ion heat fluxes, with further details in End Matter.

Although the ITG suppression is highly localized, a no-

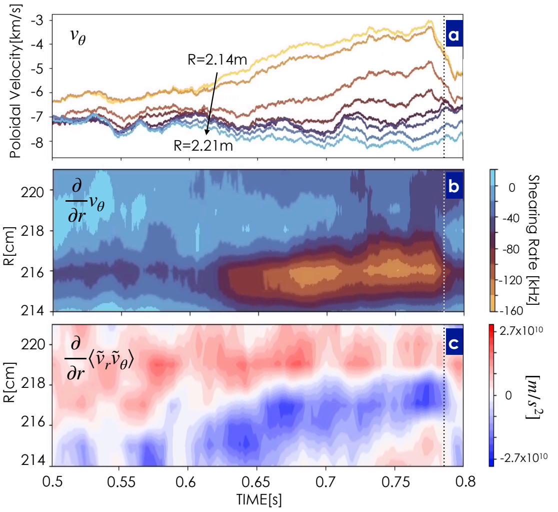

FIG. 3: The measured turbulence poloidal flow v_θ from 2.14 m to 2.21 m in (a). The negative sign in (a) indicates the ion diamagnetic drift direction. The spatial and temporal evolution of shearing rate of poloidal flow $\partial v_\theta/\partial r$ (b) and the RS force in (c).

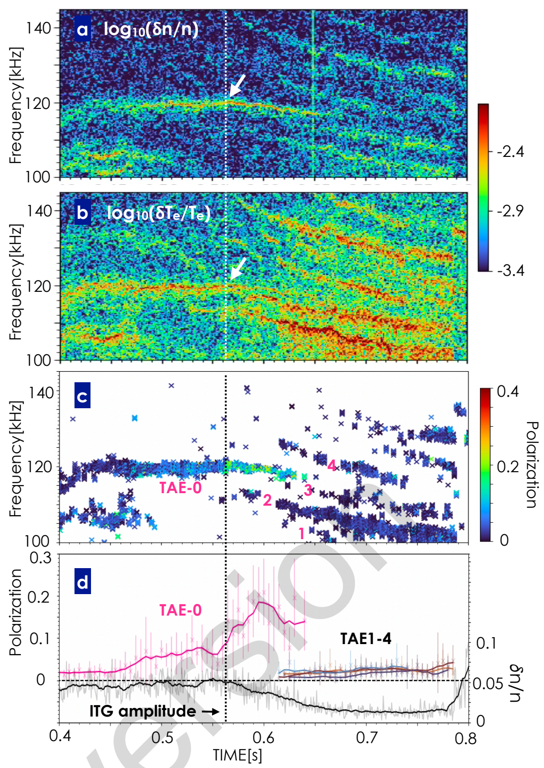

FIG. 4: The $\delta n/n$ and $\delta T_e/T_e$, measured by BES and ECE at nearly the same (R, Z) locations are shown in (a) and (b), respectively. (c) The polarization of all TAEs as function of frequency and time. (d) The time evolution of polarization of five TAEs, labeled as 0,1,2,3 and 4 in (c), along with the time evolution of ITG amplitudes, integrated over the corresponding frequency band.

ticeable improvement in plasma confinement is observed. Figure 1(c) shows a clear increase of electron temperature (T_e) at $R = 2.164$ m, measured by electron cyclotron emission (ECE) [33], despite constant neutral beam heating power. The impact of ITG on T_e becomes particularly evident upon its reappearance, which is marked by a sharp drop of T_e by $\sim 30\%$ at ~ 0.8 s. Corresponding changes are also seen in core T_e at $R = 1.96$ m and edge carbon temperature at $R = 2.12$ m, measured by charge exchange spectroscopy [34], as well as in the stored energy. In a well-diagnosed shot, seven additional high-resolution ECE channels, aligned with the localized ITG suppression region, observe T_e profiles indicative of internal transport barrier (ITB) formation. In all shots with localized ITG suppression, ITB formation occurs at the locations where ITG is suppressed, and the beneficial effect extends much more broadly. For example, a clear increase in T_e from ~ 2.17 m to ~ 2.0 m is observed in the experiment (see Figs. 9(e) and 9(f) in the End Matter).

It is well known that shear flow and the RS force often play an essential role in suppressing turbulence [35, 36]. To evaluate their roles in this case, the poloidal and radial flow velocities, v_θ and v_r, are obtained with high temporal and spatial resolution by tracking the movement of turbulence eddies in a series of BES images, using a velocimetry technique [37–39]. In similar plasma shots, the poloidal group velocity of the turbulence eddies studied here was previously shown to agree well with the measured $E\times B$ drift velocity over the radial range of $r/a \sim 0.6$ to 1.0 [40]. Figure 3(a) shows the Z-direction averaged v_θ at eight radial locations. From ~ 0.6s, v_θ begins to accelerate in the electron diamagnetic drift direction within the radial range of 2.14 m to 2.17 m ($r/a \sim 0.65$ to 0.72). At more outward radial positions, a slight increase in v_θ is observed in the ion diamagnetic direction. This results in an enhanced shear flow layer, with a shearing rate reaching up to 160 kHz, as shown in Fig. 3(b). The shear flow layer slowly expands outwards and then abruptly diminishes after ~ 0.78 s. The evolution of this shear flow (see Fig. 3(b)) is temporally and spatially correlated with the development of the TAEs with high-amplitudes and narrower radial structures, shown in Fig. 2(a), and is anti-correlated, in both time and space, with ITG dynamics, presented in Fig. 2(b). The ITG correlation rate, which characterizes how quickly turbulent eddies lose their radial coherence, is quantified by BES. At 2.14 m, the correlation rate is found to be ~ 100 kHz over the time period of 0.5 s to 0.6 s. At 2.17 m, it is 140 kHz from 0.5 s to 0.7 s. These values are smaller than and/or comparable to the measured flow shearing rate, suggesting that flow shear decorrelates turbulent eddies and suppresses the ITG.

The RS force, defined as $\frac{\partial}{\partial r}\langle\tilde{v}_r\tilde{v}_\theta\rangle$, is calculated from the measured fluctuating components of v_r and v_θ, averaged over every 3 ms. Figure 3(c) shows the RS force is negative in the radial range of 2.14 m to 2.17 m, qualitatively consistent with the observed acceleration of v_θ in the electron diamagnetic direction. Moreover, the RS force exhibits an outward radial shift, closely matching the temporal and spatial evolution of shear flow layer in Fig. 3(b).

An intriguing detail is that ITG mitigation begins from ~ 0.57 s, as seen from Fig. 2(b) and the integrated $\delta n/n$ over the relevant frequency range, shown as the black line in Fig. 4(d). This occurs ~ 30 ms earlier than the increase in shear flow at 0.6 s, as seen from Fig. 3(b). At the same time, figure 4(a) shows an increase of TAE-induced $\delta n/n$, measured by BES, while, at the same position, ECE detects a decrease in $\delta T_e/T_e$ (see dashed lines and the arrows in Figs. 4(a) and (b)). This contrasting behavior signals a sudden change in TAE's polarization [41]. Here, polarization is defined as $|\delta\phi_\parallel|/(|\delta\phi_\parallel| + |\delta\psi|)$, where $\delta\phi_\parallel$ is the effective parallel electric potential, and $\delta\psi$ is the scalar potential. A polarization value of zero, i.e., $\delta\phi_\parallel = 0$, corresponds to a pure shear Alfvén wave (SAW), while a value of one, i.e., $\delta\psi = 0$, indicates a purely electrostatic mode.

The polarization is calculated from the measured $\delta T_e/T_e$, $\delta n_e/n_e$, and plasma profiles using a gyrokinetic formulation (see Eq. (7) of [41]) and the results are shown in Fig. 4(c). It is found that the dominant single TAE initially exhibits strong SAW polarization from ~ 0.4 s. However, around 0.57 s, its polarization rapidly increases towards ~ 0.25, indicating a significant departure from SAW behavior and coinciding with the onset of ITG mitigation in Fig. 4(d). As the up-shift of polarization occurs, TAEs with pure SAW polarization (labeled as TAE1-4) begin to grow and eventually become the dominant instabilities, as shown in Figs. 4(a) and (b). The significant polarization difference can also be directly observed by the notably larger $(\delta T_e/T_e)/(\delta n_e/n_e)$ ratios associated with TAEs (labeled as TAE1-4), compared to that from the earlier single TAE (labeled as TAE-0).

Systematic experimental investigation demonstrates that robust and reproducible ITG suppression via nonlinear evolution of TAE requires a sufficiently strong drive. In DIII-D, strong drive of TAEs is achieved via a large population of fast ions on passing orbits [42, 43], low electron density, and elevated q. For example, under the identical plasma equilibria, NBI heating scenarios, current ramp-up rates, and nearly identical q profiles, an increase in n_e, i.e., reducing TAE drive, prevents the ITG suppression. Conversely, enhancing TAE drive by elevating q profiles and lowering n_e significantly extends the ITG suppression periods, leading to formation of an ITB. Details of these two examples are given in the End Matter, underscoring the critical role of TAE drive in ITG suppression.

Discussion – Several aspects of the observations challenge the traditional theoretical definition of TAEs. For example, the $n = 4$ single TAE gradually evolves from a predominantly SAW polarization at 0.4 s to a mixed SAW/acoustic polarization, as shown in Fig 4(c). In addition, coherent waves during ITG suppression exhibit very narrow radial structures, i.e., only a few cm wide, as shown in Fig. 2(a). Nevertheless, we empirically classify these fluctuations as TAE instabilities, based on the following considerations: (1) both these coherent waves and the early stage of single TAE exhibit SAW polarization; (2) their excitation correlates to the conditions of strong TAE drive, as discussed above; (3) the toroidal mode numbers are typical for TAEs in DIII-D; (4) the frequencies fall within the TAE bands and scale with the Alfvén velocity.

Mean flows and zonal flows are both zero-frequency, with zonal flows exhibiting finite spectral broadening near zero frequency and a finite radial wave number k_r, and both are known to affect the turbulence dynamics [44]. ITG-driven zonal flows can nonlinearly upshift the critical T_e gradient for ITG destabilization, a phenomenon known as 'Dimits Shift' [45, 46]. Zonal flows driven by TAE and fishbone have been numerically observed in FAR3D code and GTC codes [47], and are invoked to explain the confinement improvement in JET [25] and DIII-D [18]. Similar low-k turbulence suppression via shear flows generated by non-ambipolar fast ion transport has been reported in LHD [16] and simulated in [48]. In our experiment, increased flow shear near zero frequency is sufficient to stabilize the ITG. However, due to the localized ITG suppression and a narrow radial decorrelation length, distinguishing mean flows from zonal flows via k_r in experiment is not possible. Nevertheless, the data suggest that the poloidal flow is modified by TAE waves through the MX and RS forces. Note that a theoretical framework describing how MX and RS are generated by a group of TAEs with different n, as observed in experiments, is currently lacking. The most closely related theory to date considers the MX and RS generated by a single-n TAE, as formulated in Equation (10) of [14]. Encouragingly, the key experimental findings align well with key elements of the theory: (1) Theory predicts that poloidal flow is generated by TAEs only when they deviate from a pure SAW; otherwise, MX and RS cancel each other out. This is consistent with the measurement. (2) Theory also suggests that the imbalance between MX and RS force is pronounced only when TAE exhibits fine-scale radial structure with large amplitudes, as observed in experiment. (3) Experimentally, although MX force has not been directly measured, figure 4(b) shows that the decrease in δT_e for the single TAE after ~ 0.57 s implies reduced local magnetic fluctuation, i.e., $\delta T_e \propto \delta\psi$, while Fig. 3(c) demonstrates an increase in RS force. Together, these observations suggest an imbalance of RS and MX stress forces.

It is important to note that, in the DIII-D tokamak, full suppression of ITG is observed only when the TAE drive exceeds a certain threshold, a key condition for triggering full ITG suppression. One possible interpretation is that the intensity of zonal flows scales with the square of the TAE amplitude [49]. These flows can, in turn, modify TAE polarization, further enhancing the imbalance between MX and RS forces and thereby driving poloidal flow, thus establishing a positive feedback loop. It also facilitates nonlinear wave-wave coupling to drive more TAEs with different n. On the other hand, the requirement of TAE drive to exceed a certain threshold suggests that direct energy transfer from ITG to marginally stable TAE, a mechanism discovered in simulation [50], is not the dominant mechanism in this particular case, since it is less likely to exhibit a sharp threshold dependence. Other potential effects on ITG stability are also excluded: (1) fast ion dilution effects [22, 23]. TRANSP predicts a slight decrease of fast ion fraction by $\sim 2\%$ across the ITG suppression phase, due to a slight increase of n_e at constant neutral beam injection in Fig. 1(d). (2) Profile changes. Using measured plasma profiles and equilibrium, CGYRO finds similar linear growth rates across the suppression period without taking flow into account.

A final remark is that the strong TAE drive in this experiment leads to substantial fast ion transport. But at a comparable levels of fast ion transport in this series of experiments, a slight increase in TAE drive above threshold triggers the bifurcation in ITG behavior, from non-suppression to full suppression, resulting in a clear improvement of thermal plasma performance, especially at large radii. An intriguing concept for future reactors, suggested by this experiment, is the use of Alfvén antennas to externally excite AEs near the plasma edge, where the α particle population and associated losses could be low. By generating targeted TAE spectra, it may be possible to form transport barriers at large radii on demand.

The authors thank Liu Chen and Zhiyong Qiu for critical discussions. This material is based upon work supported by the U.S. Department of Energy, Office of Science, Office of Fusion Energy Sciences, using the DIII-D National Fusion Facility, a DOE Office of Science user facility, under Award(s) DE-FC02-04ER54698, DE-SC0020337, DE-FG02-08ER54999, DE-SC0020287, DE-SC0015878, DE-FG02-97ER54415, DE-SC0014664.

[1] W. Horton, Rev. Mod. Phys. 71, 735 (1999).
[2] G.R. Tynan, A. Fujisawa and G. McKee Plasma Phys. Control. Fusion 51, 113001 (2009).
[3] W.W. Heidbrink and G.J., Sadler, Nucl. fusion 34, 535 (1994).
[4] A. Fasoli, C. Goremnzano, H.L. Berk et al., Nucl. Fusion 47, S264 (2007).
[5] B.N. Breizman and S.E. Sharapov, Plasma Phys. Controlled Fusion 53, 054001 (2011).
[6] K. Toi, K. Ogawa, M. Isobe et al., Plasma Phys. Controlled Fusion 53, 024008 (2011).
[7] N.N. Gorelenkov, S.D. Pinches, K. Toi, Nucl. Fusion 54, 125001 (2014).
[8] K. Mcclements and E.D. Fredrickson, Plasma Phys. Controlled Fusion 59, 053001 (2017).
[9] Y. Todo, Reviews of Modern Plasma Physics (2019) 3:1 (2019).
[10] Y. Todo, H.L. Berk and B.N. Breizman, Nucl. Fusion 50, 084016 (2010).
[11] L. Chen and F. Zonca, Phys. Rev. Lett 109, 145002 (2012).
[12] F. Zonca et al., Plasma Phys. Control. Fusion 57, 014024 (2015).
[13] Z. Qiu, L. Chen and F. Zonca Phys. Plasma 23, 090702 (2016).
[14] Z. Qiu, L. Chen and F. Zonca Nucl. Fusion 57, 056017 (2017).
[15] A. Di Siena et al., Phys. Rev. Letts 127, 025002 (2021).
[16] X.D. Du et al., Phys. Rev. Lett 114, 155003 (2015).
[17] X.D. Du et al., Nucl. Fusion 56, 016002 (2016).
[18] G. Brochard et al., Phys. Rev. Lett 132, 075101 (2024).
[19] G. Brochard et al., Nucl. Fusion 65, 016052 (2025).
[20] S. Mazzi et al., Nature Physics 18, 776 (2022).
[21] H. Han et al., Nature 609, 269 (2022).
[22] D. Kim et al., Nucl. Fusion 64, 066013 (2024).
[23] T.S. Hahm, G.J. Choi, S.J. Park, Y.-S Na Phys. Plasma 30, 072501 (2023).
[24] G.J. Choi et al., Nucl. Fusion 64, 016029 (2024).
[25] J. Garcia et al., Nature Communications 15, 7846 (2024).
[26] J. Ruiz Ruiz et al., Phys. Rev. Lett. 134, 095103 (2025).
[27] Qinghao Yan and P.H. Diamond, Nucl. Fusion 65, 116034 (2025).
[28] G.R. Mckee, R. Ashley, R. Durst, R. Fonck, M. Jakubowski, K. Tritz, K. Burrell, C. Greenfield, and J. Robinson, Rev. Sci. Instrum. 70, 913 (1999).
[29] G. R. McKee,b R. J. Fonck, M. W. Shafer, I. U. Uzun-Kaymak, and Z. Yan Rev. Sci. Instrum. 81,10D741 (2010).
[30] E.J. Strait Rev. Sci. Instrum. 77 023502 (2006).
[31] M.W. Shafer et al., Rev. Sci. Instrum. 77, 10F110 (2006).
[32] J.Candy, E.A. Belli and R.V. BravenecA high-accuracy Eulerian gyrokinetic solver for collisional plasmas Journal of Computational Physics 324, 73 (2016).
[33] M. E. Austin and J. Lohr, Rev. Sci. Instrum. 74, 1457 (2003).
[34] C. Chrystal, K. H. Burrell, B. Grierson, S.R. Haskey, R.J. Groebner and D. Kaplan, Rev. Sci. Instrum. 87, 11E512 (2016).
[35] L. Schmitz Nucl. Fusion 57, 025003 (2017).
[36] Z. Yan, G.R. McKee, R. Fonck, P. Gohil, R.J. Groebner and T.H. Osbonrne, Phys. Rev. Lett 112, 125002 (2014).
[37] G. M. Quénot, J. Pakleza, and T. A. Kowalewski, Exp. Fluids 25, 177 (1998).
[38] G. R. McKee, R. J. Fonck, D. K. Gupta, D. J. Schlossberg, M. W. Shafer, C. Holland, and G. Tynan, Rev. Sci. Instrum. 75, 3490 (2004).
[39] F.O. Khabanov et al., Nucl. Fusion 64, 126056 (2024)
[40] G. R. McKee, R. J. Fonck, D. K. Gupta, D. J. Schlossberg, M. W. Shafer, R. L. Boivin, and W. Solomon, J. Plasma Fusion Res. 2, S1025 (2007)
[41] X.D. Du et al., Phys. Rev. Letts 132, 215101 (2024).
[42] R.B. White et al., Plasma Physics and Controlled Fusion 52.4, 045012 (2010).
[43] C.S. Collins et al., Nucl. Fusion 57, 086005 (2017).

[44] P.H. Diamond S-I Itoh, K. Itoh and T.S. Hahm, Plasma Phys. Control. Fusion 47, R35R161 (2005).
[45] A.M. Dimits, T. Williams, J. Byers and B. Cohen, Phys., Rev. Lett. 77, 71(1996).
[46] A.M. Dimits et al., Phys. Plasmas 7, 969 (2000).
[47] Lin Z, Hahm T, Lee W, Tang W and White R, Science 281 1835 (1998)
[48] J. Varela et al., Nucl. Fusion 65, 026002 (2025).
[49] L. Chen and F. Zonca, Rev. Mod. Phys. 88, 015008 (2016)
[50] A. Di Siena et al., Nucl. Fusion 59, 124001 (2019).

End Matter

Beam emission spectroscopy imaging system – The beam emission spectroscopy system (BES) consists of an 8×8 array, covering a radial range from 2.142 m to 2.208 m and a vertical range from -0.042 m to 0.065 m. The vertical pairs of BES channels are nearly aligned with flux surfaces, as shown in Fig. 5(a). The images of turbulence eddies at ~ 0.5 s and ~ 0.7 s, corresponding to the times before and during the ITG suppression, are shown in Fig. 5(b1) and (b2). As seen in Fig. 5(b1), the poloidal wave number k_θ before ITG suppression is about 0.8 cm^{-1}. After the ITG suppression, in the region of $\sim R = 2.17$ m to ~ 2.21 m, the eddies exhibit a tilted structure. It should be noted that toroidicity-induced Alfvén eigenmodes (TAE) and turbulence are distinguished by the phase difference $\Delta\phi$ between poloidally separated BES channels. For low-k turbulence, $\Delta\phi$ increases approximately linearly with frequency owing to the broad k_θ spectrum, whereas for TAE, $\Delta\phi \approx 0$ since the poloidal wavelength greatly exceeds the channel separation.

Identification of low-k turbulence – A linear gyrokinetic calculation using CGYRO, based on experimentally measured plasma profiles and equilibrium, is performed to identify the observed turbulence in Fig. 1. The simulation finds the modes are linearly unstable over a broad range of $k_\theta\rho_s > 0.2$, peaking at $k_\theta\rho_s \sim 0.4$, i.e., $k_\theta \sim 1.1$ cm^{-1} and $\rho_s \sim 0.35$ cm and have a real frequency of ~ 20 kHz in the ion diamagnetic drift direction. A parameter scan shows that the growth rate increases with steeper ion temperature gradients. The calculated linear growth rate spectra are used to determine the electron and ion heat fluxes by applying the quasi-linear approximation using SAT2 [Staebler Nucl. Fusion 2021]. The result shows that the heat flux is primarily driven by modes in the range $k_\theta \sim 0.8$ to 1.4 cm^{-1}, with comparable contributions from electrons and ions, as shown in Fig. 6. In comparison, the observed dominant k_θ before turbulence suppression is ~ 0.8 cm^{-1}, decreasing to ~ 0.53 cm^{-1} at $R = 2.18$ m, when turbulence is suppressed at $R = 2.14$ m (see Figs. 5(b1) and (b2)). This qualitatively suggests that the observed turbulence is ion temperature gradient mode (ITG). It should be emphasized that a quantitative comparison of ITG k_θ spectra between CGYRO and experimental data requires nonlinear simulations including cross-scale interactions among TAE, ITG and zonal flows, which remain for future work.

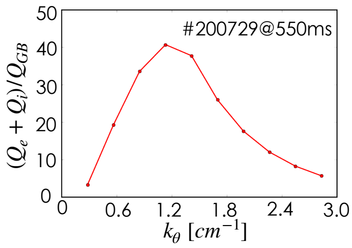

FIG. 6: Gyro-Bohm-normalized heat fluxes, as the function of poloidal wavenumber k_θ for CGYRO calculations that use the experimentally measured plasma profiles and equilibrium in shot 200729 at 550 ms.

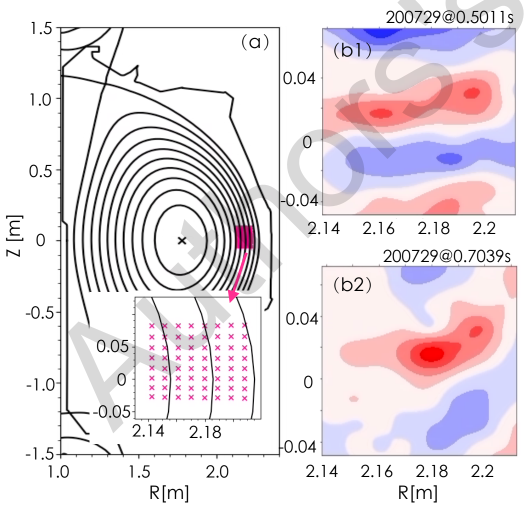

FIG. 5: (a) Viewing geometry of the BES system overlaid on the upper single-null plasma equilibrium. Examples of turbulent eddies measured by BES before ITG suppression and during ITG suppression are shown in (b1) and (b2), respectively. The red and blue bands stand for the crest and trough of the fluctuations measured by the BES system.

Toroidal mode number n – The toroidal mode number n is determined from the phase variation over an array of toroidal magnetic loops that are located on the outer midplane of the torus. Figure 7 shows the best-fitted n at different frequencies and times. Note that magnetic loops detect magnetic fluctuations at the wall, generated by the plasma instabilities across all radii, whereas BES measures the local density fluctuation.

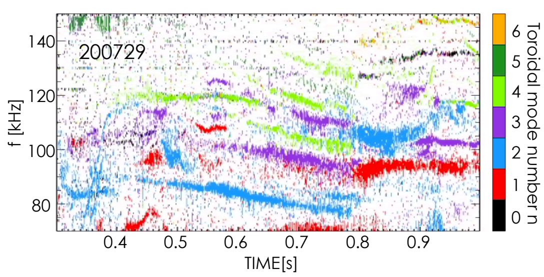

FIG. 7: Time evolution of frequency spectra for toroidal mode numbers, determined by phase variation of a toroidal array of magnetic loops.

ITG suppression vanishes under weak TAE drive – A comparative experiment is performed to investigate the role of TAE drive in the nonlinear evolution of TAE and associated ITG suppression. The results are shown in Fig. 8. In both discharges, the plasma equilibria, current ramp-up rate and neutral beam heating scenario are kept identical, while the electron density is increased by $\sim 30\%$ to reduce the fast ion drive. The q profiles, reconstructed by EFIT code with MSE constraints, show reasonable agreement between these two cases at 0.62 s, 0.66 s and 0.7 s, as seen from Figs. 8(a1)-(a3). The radial locations of ITG suppression are indicated by vertical dotted lines. It is found that, in the low-density case, i.e., stronger TAE drive, the system evolves into ITG suppression [see Figs. 8(b1) and (b2)]. In contrast, in the higher-density case, i.e., weaker TAE drive, ITG suppression is not achieved [see Figs. 8(c)].

ITG suppression extends with strong TAE drive – An experiment is conducted to examine whether the ITG suppression window can be extended by increasing the TAE drive. The results are shown in Fig. 9. The

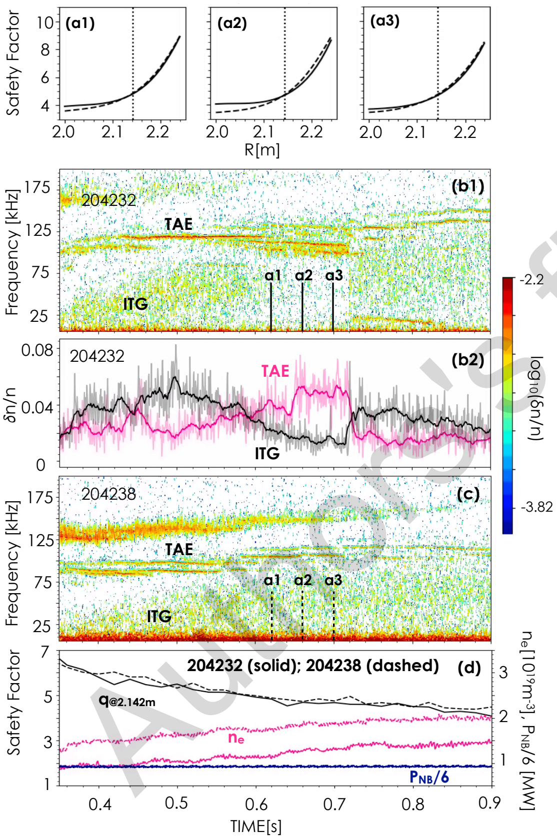

FIG. 8: Time evolution of (a1a3) q-profiles at 0.62, 0.66, and 0.70 s for shots 204232 (solid) and 204238 (dashed), with dotted lines marking the ITG suppression region. Frequency spectra of $\delta n/n$ at $R = 2.142$ m for shot 204232 (b1) and shot 204238 (c). (b2) Time evolution of ITG and TAE amplitudes for shot 204232. (d) Time evolution of n_e, q at $R = 2.142$ m, and injected beam power P_{NB} for both shots.

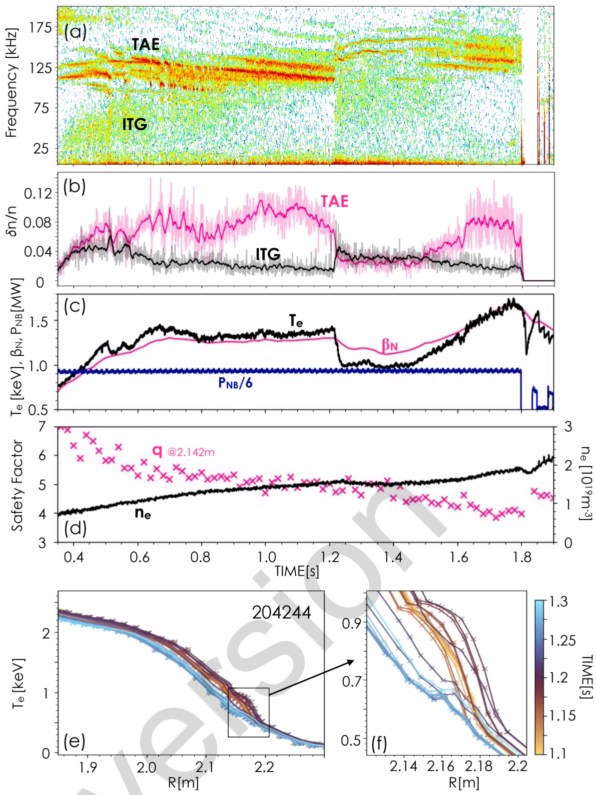

FIG. 9: (a) Frequency spectra of $\delta n/n$ at $R = 2.142$ m for shot 204244 (colormap as in Fig. 8). Time evolution of ITG and TAE amplitudes in (b), T_e, β_N, and P_{NB} in (c), n_e and q at $R = 2.142$ m in (d). (e, f) T_e profiles from 1.1 - 1.3 s and expanded view of the boxed region.

drive is enhanced by reducing the current ramp-up rate from 363 kA/s (shot 204232) to 220 kA/s (shot 204244), thereby sustaining elevated q for a longer duration. In addition, the electron density is lowered by 5 - 10%, relative to shot 204232, with the same neutral beam heating. Under these conditions, ITG suppression is observed from $\sim$ 0.85 s to $\sim$ 1.2 s, extending the duration from $\sim$ 120 ms in shot 204232 [Fig. 8(b1)] to $\sim$ 350 ms, as seen from Fig. 9(a). Importantly, a second ITG suppression window appears after 1.45 s, persisting until all of the neutral beams switch off at 1.8 s and TAEs disappear.

In both suppression windows, local ITG suppression produces a measurable impact on the global confinement, as reflected in the normalized beta β_N in Fig. 9(c). Notably, a sudden drop in T_e occurs at 1.2 s, coinciding with the loss of ITG suppression, despite nearly constant n_e and neutral beam heating power. Seven high-resolution ECE channels with a radial resolution of $\sim$ 1 cm are aligned to the radii where local ITG suppression is observed. Figure 9(e) and (f) show that the T_e profiles exhibit an internal transport barrier shape during ITG suppression, with the subsequent T_e drop corresponding to a collapse of the transport barrier when the ITG reemerges.